Published in final edited form as:
Angiogenesis. 2010 June ; 13(2): 189–202. doi:10.1007/s10456-010-9166-0.

Theragnostics for tumor and plaque angiogenesis with perfluorocarbon nanoemulsions

G. M. Lanza, **P. M. Winter**, **S. D. Caruthers**, **M. S. Hughes**, **Grace Hu**, **A. H. Schmieder**, and **S. A. Wickline**
Division of Cardiology, Department of Medicine, Washington University Medical School, 4320 Forest Park Ave, Suite 101, St. Louis, MO 63108, USA

G. M. Lanza: greg@cvu.wustl.edu

Abstract

Molecular imaging agents are extending the potential of noninvasive medical diagnosis from basic gross anatomical descriptions to complicated phenotypic characterizations based upon the recognition of unique cell-surface biochemical signatures. Although originally the purview of nuclear medicine, “molecular imaging” is now studied in conjunction with all clinically relevant imaging modalities. Of the myriad of particles that have emerged as prospective candidates for clinical translation, perfluorocarbon nanoparticles offer great potential for combining targeted imaging with drug delivery, much like the “magic bullet” envisioned by Paul Ehrlich 100 years ago. Perfluorocarbon nanoparticles, once studied in Phase III clinical trials as blood substitutes, have found new life for molecular imaging and drug delivery. The particles have been adapted for use with all clinically relevant modalities and for targeted drug delivery. In particular, their intravascular constraint due to particle size provides a distinct advantage for angiogenesis imaging and antiangiogenesis therapy. As perfluorocarbon nanoparticles have recently entered Phase I clinical study, this review provides a timely focus on the development of this platform technology and its application for angiogenesis-related pathologies.

Keywords

Perfluorocarbon; Nanoparticles; Angiogenesis; Ultrasound; MRI; Nuclear; Fumagillin; Theragnostic; Molecular imaging; Drug delivery

Introduction

Folkman first seriously proffered the concept of angiogenesis as a keystone in the treatment of cancer, and now many other diseases, in 1971 [1]. Since that time, this fundamental premise has garnered experimental and clinical support leading to the subsequent approval of bevacizumab, a humanized monoclonal antibody directed against vascular endothelial growth factor (VEGF) in combination with chemotherapy [2–4]. Subsequently, two additional antiangiogenic therapies have been approved for marketing by the Food and Drug Administration (FDA), sorafenib [5] and sunitinib [6], which are oral small-molecule tyrosine kinase inhibitors effective against multiple receptors of this class including VEGF and platelet-derived growth factor (PDGF). These first-generation antiangiogenic therapeutic approaches have demonstrated survival benefit in subsets of patients, but their

---

Correspondence to: G. M. Lanza, `greg@cvu.wustl.edugreg.lanza@me.com`.

high cost and notable adverse side-effect risk [7, 8] have fueled alternative research and development efforts, including nanomedicine approaches to the problem.

Viable clinical solutions to antiangiogenesis therapy must minimally provide equivalent or better efficacy with improved safety for a lower cost in order for this medical strategy to be used across the spectrum of potential pathologies. Clinical evidence to date suggests that some patients will benefit markedly, while many have little or no significant improvement, indicating an unmet need to more effectively identify those candidates with the highest treatment benefit potential. Moreover, rapid advances in cost-effective genomic profiling and sensitive early detection of high-risk biomarkers for cancer and early atherosclerosis will challenge the medical community to assess and treat asymptomatic patients early in the natural history of the disease process. Current diagnostic imaging techniques are inadequate for sensitive and specific detection and characterization of nascent pathology, and the majority of medical therapies, particularly within the realm of oncology, are more severe than the underlying disease at that stage of progression. Emergent noninvasive biomedical imaging approaches that combine sensitive, specific, and quantitative microanatomic/biochemical/functional characterization of pathology with the added capacity to deliver effective therapy, particularly antiangiogenic treatment, with fewer adverse effects are in development. This new class of agents has acquired the moniker “theragnostic” (i.e., therapy and diagnostic).

Clinical techniques are available to help stage and monitor response to cancer treatments and include dynamic contrast-enhanced magnetic resonance imaging (DCE-MRI) and ^{18}fluorodeoxyglucose (^{18}FDG) positron emission tomography (PET). However, these techniques have not proved effective in stratifying patients into treatment regimens based on tumor neovascularity. Radiolabeled arginine-glycine-aspartic acid (RGD) peptides and antibodies, particularly directed to the $\alpha_v\beta_3$-integrin, have been used to target and characterize tumor angiogenesis by microPET [9] and single photon emission computed tomography (SPECT) [10]. However, these small molecules readily permeate into the tumor and like ^{18}FDG, bind many cell types, including activated macrophages and proliferating tumor cells, which diminishes the signal specificity for angiogenesis *per se*. DCE-MRI can detect changes in tumor microvasculature permeability to MR blood pool contrast agents [11, 12], and some studies have correlated these kinetic estimates with traditional measures like microvessel density (MVD), but initial clinical trials have yielded inconsistent results due to either insufficient standardization of the endpoints or technique issues [13, 14].

Among a cadre of MR molecular imaging agents that have been invented and studied over the last several years, lipid-based paramagnetic particles, such as perfluorocarbon (PFC) emulsions [15–17], liposomes [18–21], or micelles [22] targeted to biomarkers by antibody, small peptides or peptidomimetics, have shown particular effectiveness in monitoring $\alpha_v\beta_3$-integrin endothelial expression before and after treatment. Of these, PFC nanoparticles have proven to be a robust theragnostic technology for quantitative MR monitoring and antiangiogenic treatment.

Perfluorocarbon (PFC) nanoparticles (NP) are a multi-functional theragnostic technology with versatile potential demonstrated in a variety of preclinical animal cancer and atherosclerotic models. These particles (250 nm) encapsulate a PFC core with a monolayer of phospholipids. The biocompatibility of perfluorooctylbromide core is well documented, even at large doses, with no toxicity, carcinogenicity, mutagenicity, or teratogenic effects, and it is eliminated unmetabolized through exhalation with a 3-day biological half-life [23]. PFC NPs are constrained within the vasculature during the targeting phase, which makes them ideal candidates for specific homing to intravascular biosignatures, such as integrins, selectins, or adhesion molecules.

PFC nanoparticle technology

Targeting angiogenesis with PFC nanoparticles

Neovessel formation, i.e., angiogenesis expansion, is an important signature of aggressive cancers and progressive atherosclerosis. One molecular biosignature, $\alpha_v\beta_3$-integrin, has garnered prominent attention for angiogenic targeting applications because it is expressed on the luminal surface of activated endothelial cells but not on mature quiescent cells. Unfortunately, the $\alpha_v\beta_3$-integrin, a heterodimeric transmembrane glycoprotein, is not only presented by neovasculature endothelial cells but also expressed by numerous cell types including macrophages [24], platelets [25], lymphocytes [25], smooth muscle cells [26], and tumor cells [27, 28]. Fortunately, the constraint of PFC NPs to the vasculature precludes significant interaction with these nonendothelial integrin-expressing cells, which greatly enhances neovascular target specificity [29].

While a variety of peptide-based homing ligands have evolved around the fundamental arginine-aspartate-glycine (RGD) motif, first introduced by Ruoslahti [30], we have primarily utilized a peptidomimetic small molecule with high specificity and affinity. The $\alpha_v\beta_3$-integrin antagonist is a quinalone nonpeptide developed by Bristol-Myers Squibb Medical Imaging (US patent 6,511,648 and related patents), which was initially reported and characterized as the ^{111}In-DOTA conjugate RP478 and cyan 5.5 homologue TA145 [31]. The specificity of the $\alpha_v\beta_3$-ligand mirrors that of LM609 as assessed by staining and flow cytometry, and it has a 15-fold preference for the Mn^{2+}-activated receptor (21 nM) [31]. The IC_{50} for $\alpha_v\beta_5$, $\alpha_5\beta_1$ and GP IIbIIIa was determined to be > 10 μM (BMSMI, Billerica, MA, USA, unpublished data). The binding affinity of the PFC nanoparticle decorated with approximately 500 homing ligands is 50 pM.

Multi-modal molecular imaging with PFC nanoparticles

Targeted ultrasound imaging—*Targeted Ultrasound Imaging*

In contradistinction to individual microbubbles that have short in vivo half-lives and produce remarkable acoustic contrast, whether circulating, trapped, or targeted, ligand-targeted, nongaseous perfluorocarbon emulsions have poor inherent acoustic reflectivity [32, 33] unless concentrated upon the surfaces of tissues or membranes, which provides marked improvement in contrast signal without increasing the background level. In the first report of ultrasonic molecular imaging, marked acoustic enhancement of thrombi created by perfluorocarbon nanoparticles targeted systemically in vivo in a canine model illustrated the concept of contrast-based tissue characterization [34]. In that report, we demonstrated that perfluorocarbon nanoparticles, although too small to be detected in circulation at the low molecular imaging dosage employed, were able to persist in blood, specifically bind to pre-targeted fibrin, and generate marked acoustical enhancement of acute vascular thrombi [34].

The acoustic reflectivity of bound perfluorocarbon nanoparticles was approximated by a first-order mathematical model, i.e., an acoustic linear transmission model, which helped to elucidate the major principles governing the magnitude of acoustic reflectivity [35]. In this model, the key elements influencing spectral ultrasonic reflectivity were the effective emulsion layer: density, speed of sound, and thickness. We extensively characterized the acoustic properties of a wide variety of potential perfluorocarbons and subsequently formulated a series of perfluorocarbon compounds of varying acoustic impedance [36, 37]. In synopsis, these studies revealed that all liquid perfluorocarbon emulsions significantly increase target acoustic reflectivity when bound to a surface and the magnitude of enhancement may be manipulated by formulating nanoparticles with perfluorocarbons of different acoustic impedance. Moreover, we determined that introduction of exogenous heating accentuated the acoustic contrast of nanoparticle-targeted tissues by lowering perfluorocarbon speed of sound, which augmented the acoustic impedance mismatch and increased the surface spectral reflections [38]. Essentially, the echogenicity of nanoparticles bound to a tissue surface was analogous to the reflectivity of light by a mirror, i.e., the more complete the coating of silver grains over glass surface, the clearer the reflected image.

For thrombus where the concentration of fibrin epitopes is vast, the acoustic imaging of targeted nanoparticles is readily accomplished with traditional fundamental ultrasound approaches. However, when biomarker targets have sparse density distributions, such as in angiogenesis, complementary acoustic receivers were required and developed that were highly sensitive to the subtle changes in wave shape (i.e., the contours and ripple patterns).

Detection of molecular epitopes associated with neovasculature with integrin-targeted PFC nanoparticles presents a unique challenge for ultrasonic clinical imaging systems. Whereas subsequent investigators utilized microbubbles by virtue of their high inherent contrast, but whether a microbubble is bound, entrapped, or circulating in the background is difficult to discern directly. In contradistinction, targeted PFC nanoparticles, with much lower acoustic contrast, must be detected due to their bound accumulation in the presence of other bright echoes returned from the surrounding tissue. We approached the problem of detection of site-specific contrast through the use of signal receivers i.e., mathematical operations that reduce an entire radio frequency (RF) waveform or a portion of it to a single number based on information-theoretic quantities, such as Shannon entropy (H), or its counterpart for continuous signal (H_f) [39, 40]. These receivers appear to be sensitive to diffuse low amplitude features of the signal that often are obscured by noise or else lost in large specular echoes and, hence, not usually perceivable by a human observer.

Although entropy-based techniques have a long history in image processing for image enhancement and postprocessing of reconstructed images, the approach employed was quite different in that entropy was used directly as the quantity defining the pixel values in the image. Specifically, images are reconstructed by computing the entropy (or a limiting form of it: H_f, or $I_{f,¥}$) of segments of the individual RF A-lines that comprise a typical medical image by applying a “moving window”, or “box-car”, analysis. The computation of an entropy value for each location within an image is therefore possible, and the results can be superimposed over the conventional grayscale image as a parametric map. This approach has been integrated into current commercial ultrasound scanner on a prototype basis providing real-time direct molecular imaging [40] as opposed to inference from a differential pattern obtained pre- and post-microbubble destruction and reflow.

^{1}H T1-weighted MR molecular imaging with PFC nanoparticles—MRI offers several advantages over other clinical modalities for molecular imaging, including high resolution, noninvasiveness, high anatomical contrast, and lack of ionizing radiation. The partial volume dilution effect, which is inherent in MR imaging, has often led to the failure of targeted contrast agents in vivo. Initial attempts of targeted imaging with MRI focused on coupling gadolinium atoms directly to antibodies or proteins, but these approaches delivered insufficient paramagnetic material to effectively decrease local relaxation times and provided inadequate MR signal enhancement on T1-weighted images at typical clinical field strengths. Later, ligand-directed macromolecular constructs were used to increase gadolinium ion payload delivered to each binding site, which amplified the MR contrast enhancement to acceptable levels. The two principal features of successful targeted paramagnetic contrast agents are the number of gadolinium ions delivered or accumulated at each binding site, i.e. the paramagnetic payload, and the relaxivity influence provided by each gadolinium atom.

The first-generation paramagnetic PFC nanoparticles (250 nm) incorporated a lipophilic chelate, i.e., gadolinium-diethylene-triamine-pentaacetic acid bis-oleate (Gd-DTPA-BOA, metal oriented outward) into the surfactant layer. These relatively large paramagnetic constructs have high relaxivity per gadolinium atom (ion-based relaxivity) due to the slower tumbling rate of the particle in comparison with free gadolinium-diethylene-triamine-pentaacetic acid (Gd-DTPA) and support high surface payloads of metal, typically 100,000 gadolinium ions per 250 nm particle, providing extremely high relaxivity per particle (particle-based relaxivity). By varying the payload of Gd-DTPA-BOA chelate on the nanoparticle surface, the particulate r1 relaxivity at 1.5 T was increased from 10 to 40 mol% [15]. Subsequently, we demonstrated that repositioning the Gd-DTPA chelate slightly above the lipid surface of the nanoparticle markedly enhanced the r1 and r2 relaxivities by up to 300% [41].

The requisite extended biological half-life of lipophilic gadolinium chelates demands a complexation with minimal toxicity potential through transmetallation. This led to the development of gadolinium-methoxy-tetraazacyclodode cane-tetraacetic acid (Gd-MeO-DOTA)-phosphatidyletha-nolamine (PE)-based nanoparticles, which retained the improved high relaxivity achieved Gd-DTPA-PE PFC nanoparticles [42]. Moreover, the transmetallation of gadolinium was markedly diminished for the macrocyclic DOTA constructs in the presence of excess $ZnCl_2$, in comparison with the linear chemistry of the DTPA chelate, which was further compromised of the loss of coordination bond(s) imparted by the lipid modification [42]. In subsequent generations of paramagnetic particles, the gadolinium chelate–lipid conjugates employed retained an above surface localization of the DOTA chelate for maximum relaxivity (US Pat. No. 6,869,591).

^{19}F imaging with PFC nanoparticles—^{19}F presents an excellent probe for quantitative MRI, which is highly enriched in perfluorocarbon nanoparticles. ^{19}F has 100% natural abundance, a spin of ½, and a gyromagnetic ratio of 40.08 MHz/T close to the that of ^{1}H (42.58 MHz/T), resulting in 83% of the sensitivity of ^{1}H [43]. In addition, the chemical shift of ^{19}F, due to its seven outer-shell electrons, is sensitive to the molecular environment of the nucleus, including oxygen tension. The ^{19}F spectroscopic signature manifests a range of > 200 ppm, [44, 45] which permits unambiguous identification of distinctive ^{19}F-containing compounds even at low field strengths. Moreover, no background exists for the ^{19}F signal in vivo, providing a unique spectroscopic signature for quantitative MRI.

The unique capability of ^{19}F MRI to directly determine the absolute quantity of ^{19}F atoms has been largely unexploited until the recent advent of PFC nanoparticle-based molecular imaging beginning in 1996 [46]. Although these targeted nanoparticles were used initially to deliver high payloads of surface gadolinium to enhance T1-weighted ^{1}H MRI as discussed above, they inherently resulted in regional deposition of ^{19}F atoms adequate for quantitative MRI. Using fibrin-targeted PFC nanoparticles, the bound particles on the surface of fibrin clots provided enough ^{19}F atoms for MRI at 4.7 T field strength [47, 48]; later the concept was extended to a clinical scanner at 1.5 T [49]. The linear correlation between the quantity of bound ^{19}F atoms and the measured ^{19}F MR signal from functionalized PFC nanoparticles has been quantitatively mapped [48] in clot and tissue phantoms. PFOB and PFCE (perfluoro-15-crown-5-ether) nanoparticles targeted to the same biological specimen were simultaneously or selectively assessed with ^{19}F MRI at 1.5 T, illustrating the unique spectral opportunity for phenotypic characterization achievable by delineation of multiple pathological biosignatures simultaneously [49]. Subsequently, Neubauer et al. further demonstrated that paramagnetic Gd^{3+} closely bound to the surfactant of PFC NPs increased the ^{19}F r1 by fourfold, improving ^{19}F signal intensity 125% at 1.5 T [50].

Examples of ^{19}F imaging of sparse epitopes as presented by biological tissues have included detection of athero-sclerotic valve angiogenesis [51]. Angiogenic valve leaflets in hyperlipidemic rabbits following $\alpha_v\beta_3$-integrin-targeted PFC nanoparticles exhibited ~3 times higher ^{19}F signal ex vivo than similar valve leaflets in atherosclerotic animals treated with untargeted nanoparticles [51]. Potentially in vivo quantitative ^{19}F MRI using site-targeted PFC nano-particles can be complicated by background signal from unbound particles circulating in the blood pool depending on the dose, timing of imaging, and field strength (particularly above 4.7 T); however, the use of diffusion weighted ^{19}F MRI techniques to selectively suppress the ^{19}F signal from circulating nanoparticles versus the targeted bound particles eliminates this background problem [52].

PFC nanoparticles uniquely support both ^{1}H and ^{19}F imaging, which now may be performed simultaneously, and which offers many benefits in image registration, motion correction, and quantitative data calibration. Moreover, clinical dual-tuned MR systems offer unique data acquisition, which, due to the isotropic coverage of k-space, allows for multi-resolution, and therefore multi-sensitivity, reconstruction of the simultaneously acquired ^{19}F/^{1}H data. Variable k-space weighting in the reconstruction of simultaneously acquired ^{19}F/^{1}H 3D radial data allows optimizing the balance between SNR and resolution in the ^{19}F image retrospectively, while maintaining high resolution for the ^{1}H image for anatomical co-registration. This *a posteriori* approach for the choice of ^{19}F image resolution is a powerful tool because the degree of angiogenesis and corresponding signal levels are unknown a priori. Moreover, achieving absolute quantification of the ^{19}F signal requires various data corrections including the coil-specific spatial inhomogeneity of the B_1 field. To overcome this inhomogeneous measurement, B_1 correction approaches, called the "actual flip angle imaging" technique, have been reported that provide an image-based measure of the actual combined excitation and reception field map for the coil/anatomy combination. The advances in dual ^{19}F/^{1}H will enable the quantitative need for angiogenesis assessments, e.g., an angiogenic index, to be developed to stratify patients and guide medical management.

High-sensitivity: high-resolution SPECT-CT/MR molecular imaging—While numerous radiolabeled $\alpha_v\beta_3$-integrin or vitronectin antagonists, including antibodies, peptides, peptidomimetics, and disintegrins, have been explored as tumor vasculature targeting agents [9, 31, 53–60], their penetration beyond the circulation allows binding to a cadre of non-endothelial sources. In contrast, PFC NPs are constrained by size (250 nm, nominal diameter) to the vasculature, which is expected for agents greater than 120 kDa or 100 nm unless vascular integrity is significantly disrupted [29, 61].

The specific high-resolution MR molecular imaging of neovascular-rich pathology using $\alpha_v\beta_3$-paramagnetic nanoparticles in a variety of in vivo studies [16, 17, 62–65] has been discussed above, and the utility of ^{111}In $\alpha_v\beta_3$-nanoparticles to provide a high sensitivity, low-resolution signal from the tumor neovasculature has also been demonstrated [66]. However, the more clinically relevant and challenging opportunity involves the combination of ^{99m}Tc imaging and MRI to provide high-sensitivity detection with high-resolution 3D neovasculature mapping. While molecular imaging in cancer implies that tumor-related pathognomonic biomarkers are detected with high sensitivity and characterized with high resolution, the localization of occult tumors or metastases within large tissue volumes favors high-sensitivity imaging techniques, such as nuclear imaging. Unfortunately, nuclear imaging offers only low resolution (mm), which precludes pathologic characterization based on microscopic anatomical detail of nascent lesions. Incorporation of ^{99m}Tc functionality into the $\alpha_v\beta_3$-targeted gadolinium nanoparticles has been shown to provide a highly detectable nuclear signal that can further direct focused MR examination and neovascular characterization [67]. MR molecular imaging with 3D neovascular mapping using the dual modality approach demonstrated a coherent, asymmetric, patchy pattern of angiogenesis along the outer aspects of the tumor mass, consistent with an angiogenic phenotype [63].

Drug delivery with PFC nanoparticles—The unfortunate toxicities associated with anti-VEGF therapy reflect the pleiotropic physiological roles of VEGF and the unintended consequences of disrupting the pro-angiogenesis pathway via VEGF adsorption or inhibition [7]. Image-guided nanomedicine strategies directed specifically to proliferating neovascular endothelial cells with antiproliferative/antiangiogenic drugs may provide equivalent antiangiogenic effectiveness with less collateral morbidity. We have reported a novel approach to targeted drug delivery and termed it “contact facilitated drug delivery” [68] (Fig. 1a). Contact facilitated drug delivery refers to the (ATP independent) transfer of lipid surfactant components into the outer leaflet of the target cell membrane through a hemifusional complex [68–70] (Fig. 1b). It is a slow second-order process that depends upon the persistent interaction of the lipid-encapsulated nanoparticle with the target cell membrane surface. In effect, theragnostic PFC nanoparticles deliver a “kiss of death” without the typical requisite cellular internalization and subsequent drug payload escape from the endosomal compartment [69, 70]. Chemotherapeutics, such as paclitaxel [68], doxorubicin [68], rapamycin [71], fumagillin [63–65, 72], as well as toxic peptides, such as mellitin [73], and thrombolytic enzymes [74], have been effectively incorporated into the surfactant of PFC nanoparticles.

With respect to angiogenesis, fumagillin, a mycotoxin produced by *Aspergillus fumigatus*, suppresses endothelial proliferation by inhibition of methionine aminopeptidase 2 (MetAP2) [75, 76]. The antiangiogenic effectiveness of TNP-470, a water-soluble functional analogue of fumagillin, was widely demonstrated in rodents [77–80] and later studied in human clinical trials [81–85]. Anecdotal cases of complete remission of cervical cancer, regression of breast cancer, and stabilization of disease in patients with sarcoma, melanoma, and adenocarcinoma were reported. Unfortunately, TNP-470 has significant liabilities including a brief systemic half-life for itself (2 min.) and its primary metabolite AGM-1883 (6 min) [81], and the dosage required to elicit therapeutic effects also induces sudden moderately severe symptoms of neurotoxicity, including weakness, nystagmus, diplopia, and ataxia [81, 82, 85]. As shown below in preclinical models of cancer and atherosclerosis, fumagillin incorporated into $\alpha_v\beta_3$-targeted PFC nanoparticle surfactant and delivered at less than a 10,000th of the dose applied clinically suppressed neovascular proliferation with no significant adverse effects in rabbits and rodents [63–65, 72].

Studies: angiogenesis theragnostic in cancer and atherosclerosis

$\alpha_v\beta_3$-targeted fumagillin PFC nanoparticles in cancer

$\alpha_v\beta_3$-integrin-targeted paramagnetic nanoparticles were demonstrated to sensitively detect histologically corroborated angiogenic endothelium at 1.5 T in New Zealand White rabbits bearing Vx-2 tumors (<1.0 cm) implanted into the hind-limb 12 days previously [16], which confirmed and significantly extended the previous report of Sipkins et al. in the same model [18]. An in vivo competition group demonstrated markedly diminished signal relative to animals receiving the $\alpha_v\beta_3$-targeted nanoparticles. In a more challenging follow-on study, MR signal enhancement from the targeted angiogenic vasculature was apparent 0.5 h following IV administration of $\alpha_v\beta_3$-integrin-targeted PFC nanoparticles to athymic mice implanted with human melanoma xenografts (C-32, ATCC, <40 mm^3); the signal became progressively more prominent over 2 h (177%) [86] (Fig. 2). In this model as well, in vivo competition studies markedly diminished the signal from $\alpha_v\beta_3$-targeted nanoparticles, confirming homing specificity; the molecular imaging results were corroborated microscopically.

Later, $\alpha_v\beta_3$-targeted nanoparticles incorporating minute dosages of fumagillin were shown to diminish the development of neovasculature and to reduce Vx-2 tumor growth in rabbits [63] (Fig. 3). Neither nontargeted fumagillin nano-particles nor $\alpha_v\beta_3$-targeted nanoparticles without drug reduced angiogenesis or diminished tumor growth. Quantitative MR molecular imaging with $\alpha_v\beta_3$-targeted paramagnetic nanoparticles further revealed that the neovasculature was distributed predominately in the peripheral aspects of the tumor accounting for seven percent of that volume. These measures were microscopically corroborated by the co-localization of $\alpha_v\beta_3$-targeted rhodamine nanoparticles with FITC-lectin exclusively in or adjacent to the tumor capsule.

High-resolution three-dimensional neovascular maps illustrated the coherent asymmetric expression of angiogenesis as a few confluent regions of high-density neovascularity with an interspersed reticular network of enhancing voxels (Fig. 3). Large regions of the tumor surface and the interior were devoid of $\alpha_v\beta_3$-targeted paramagnetic nanoparticle signal enhancement. Both the islands of dense neovasculature and the intervening network of neovessel formation were diminished by treatment with $\alpha_v\beta_3$-targeted fumagillin nanoparticles. Interestingly, non-necrotic regions of the tumor parenchyma were associated with increased accumulation of intratumoral cytotoxic lymphocytes following $\alpha_v\beta_3$-targeted fumagillin nanoparticle treatment versus controls.

In follow-up, the utility of $\alpha_5\beta_1$-integrin as a biomarker for angiogenesis in cancer was studied in the MDA-MB-435 xenograft mouse model [65]. $\alpha_5\beta_1$-integrin, like $\alpha_v\beta_3$ integrin, is an important adhesion molecule, which regulates endothelial cell migration and survival during neovascularization [87]. $\alpha_5\beta_1$-integrin is poorly expressed on normal quiescent blood vessels, but its expression is induced on tumor blood vessels and in response to angiogenic factors [88] including basic fibroblast growth factor, interleukin-8, tumor necrosis factor-alpha, and the angiomatrix protein Del-1. While the role of $\alpha_v\beta_3$-integrin is well documented in aggressive melanoma and breast cancer metastasis, $\alpha_5\beta_1$-integrin is frequently associated with tumors of lower malignant potential in addition to aggressive carcinomas.

The molecular imaging and antiangiogenic effects of fumagillin nanoparticles targeted by a dual $\alpha_5\beta_1(\alpha_v\beta_3)$-peptidomimetic versus the $\alpha_v\beta_3$-peptidomimetic alone were investigated using 3D MR neovascular mapping. Like the $\alpha_v\beta_3$-peptidomimetic described above, the $\alpha_5\beta_1(\alpha_v\beta_3)$-integrin antagonist was a quinalone nonpeptide (PCT/US1998/012010) with an IC_{50} of 390 pM for $\alpha_5\beta_1$ and 87 nM for $\alpha_v\beta_3$ and no effective cross-reactivity with $\alpha_v\beta_5$ or GPIIbIIIa. Three-dimensional reconstructions of the MR signal enhancement revealed the sparse spatial organization of neovessels, which predominantly were confined to the tumor periphery. $\alpha_5\beta_1(\alpha_v\beta_3)$-targeted nanoparticles containing fumagillin further decreased the already small amount of neovessel enhancement to an almost negligible level, but in contradistinction to the marked decrease in tumor volume in the Vx2 model, fumagillin antiangio-genesis did not affect tumor volume in the MDA 435 animals. The effectiveness of targeted antiangiogenic therapy logically depends on the adequate expression of the neovascular biomarker and the dependence of tumor growth on the neovasculature. The MDA-MB-435 tumor model had a very sparse neovasculature, was relatively slow growing, and did not display a marked “angiogenic switch” phenotype as opposed to the Vx2. From the clinical perspective, MR angiogenic characterization of small tumors, particularly breast, lung, or colon, may better stratify patients into medical strategies involving anti-VEGF treatment dependent on the prominence of neovasculature. Perhaps, such a patient enrichment approach would yield more cost-effective benefits with less unnecessary exposure to off-target risk.

32$\alpha_v\beta_3$-targeted fumagillin PFC nanoparticles in atherosclerosis

Atherosclerotic plaque progresses from an early atheroma-tous lesion to a thin-capped vulnerable plaque through aggressive inflammatory and immune responses, comprising macrophage infiltration with necrotic core enlargement, neovascular expansion of the vasa vasorum, and intraplaque hemorrhage [89–91]. Increased plaque angiogenesis, driven by hypoxia [92], proangiogenic growth factors [93], and oxidative stress [94], portends unstable vascular disease [89, 90]. Angiogenesis is correlated with plaque rupture and is associated with the morphological features of vulnerable atheroma including macrophage infiltrated fibrous caps [89], lipid-rich cores [95], and thin-cap shoulders [89]. The preponderance of data from experimental models and human pathological samples indicates that plaque neovasculature could serve as a molecular imaging biomarker of atherosclerotic severity and cardiovascular disease risk.

The potential role of antiangiogenic therapy in the treatment of atherosclerosis has garnered increasing scientific discussion both pro [96] and con [90, 97]. While there is general agreement that angiogenesis is a prominent feature of vulnerable and ruptured plaques versus more stable fibrocalcific lesions, questions regarding the causative relationship and clinical relevance of antiangiogenic therapeutic strategies in cardiovascular disease have been raised. Many have postulated that antiangiogenesis therapy may normalize atherosclerotic plaque vasculature through neovascular pruning, which could diminish intraplaque hemorrhage frequency and promote plaque stabilization [98].

Molecular imaging of angiogenesis with $\alpha_v\beta_3$-targeted paramagnetic nanoparticles in fat-fed rabbits—In the first experiment to demonstrate molecular imaging of angiogenesis in early atherosclerosis with $\alpha_v\beta_3$-integrin-targeted paramagnetic PFC nanoparticles, male New Zealand White (NZW) rabbits were fed either 1% cholesterol or standard rabbit chow for ~80 days [62]. Cholesterol-fed rabbits received either (1) $\alpha_v\beta_3$-targeted paramagnetic nanoparticles, (2) nontargeted paramagnetic nanoparticles, or (3) pre-treatment with $\alpha_v\beta_3$-targeted nonparamagnetic nanoparticles 2 h prior to $\alpha_v\beta_3$-targeted paramagnetic nanoparticles (in vivo competitive blockade). All control-diet animals received $\alpha_v\beta_3$-targeted paramagnetic nanoparticles.

MR signal in the abdominal aorta integrated from the diaphragm to renal arteries increased after contrast injection, indicating the presence of targeted nanoparticles bound to $\alpha_v\beta_3$-integrin epitopes on the neovasculature. Aortic wall contrast enhancement was variable along the circumference and length of the aorta. However, greater signal enhancement was observed in the cholesterol-fed/targeted rabbits in practically every aortic segment. Quantification of the aortic signal enhancement among cholesterol-fed rabbits receiving $\alpha_v\beta_3$-targeted paramagnetic nanoparticles showed a 47 ±5% increase over baseline at 120 min., which was twice the enhancement appreciated in rabbits receiving the nontargeted nanoparticles. Competitive blockade of angiogenic $\alpha_v\beta_3$-integrins with targeted nonparamagnetic nanoparticles reduced the signal enhancement of $\alpha_v\beta_3$-targeted paramagnetic nanoparticles by at least 50%. The signal enhancement observed in the adjacent skeletal muscle due to nanoparticles in all treatment groups was negligible relative to that exhibited by the aortic wall.

Antiangiogenic treatment with $\alpha_v\beta_3$-targeted fumagillin nanoparticles in early atherosclerosis—The second study focused on demonstrating the effectiveness of $\alpha_v\beta_3$-targeted paramagnetic fumagillin nanoparticles in early atherosclerosis in this hyperlipidemic rabbit model. In that experiment [72], three paramagnetic nanoparticle formulations (i.e., $\alpha_v\beta_3$-targeted fumagillin nanoparticles, $\alpha_v\beta_3$-targeted nanoparticles without fumagillin, and nontargeted fumagillin nanoparticles) were studied (Fig. 4).

During baseline scanning, T1-weighted black blood images showed no gross evidence of significant plaque development within the wall of the abdominal aorta in terms of lumenal narrowing or wall thickening compared to previous experiments utilizing age-matched, nonatherosclerotic rabbits. As noted in the previous study, MRI signal enhancement from the aortic walls of atherosclerotic rabbits injected with $\alpha_v\beta_3$-targeted nanoparticles, both with and without fumagillin, displayed a patchy distribution, with generally higher levels of angiogenesis near the diaphragm. MRI signal enhancement averaged over all imaged slices was identical for $\alpha_v\beta_3$-targeted nanoparticles with and without fumagillin.

One week after nanoparticle treatment, the residual angiogenic activity within the aortic wall was reassessed. The aortic wall signal intensity at baseline was identical for all groups at the time of treatment and at the 1-week follow-up, confirming that the paramagnetic nanoparticles administered 1-week prior were undetectable. MRI enhancement from angiogenic vasculature 1 week following $\alpha_v\beta_3$-targeted fumagillin nanoparticle treatment was markedly reduced in both spatial distribution and signal intensity. By comparison, the MR signal enhancement 1 week after treatment with $\alpha_v\beta_3$-targeted nanoparticles lacking fumagillin was undiminished. Treatment with nontargeted fumagillin nanoparticles did not significantly inhibit angiogenesis compared to $\alpha_v\beta_3$-targeted nanoparticles without fumagillin.

Abdominal aorta sections obtained 1-week after nanoparticle treatment revealed mild, heterogeneously distributed intimal thickening consistent with very early atherosclerotic neointimal development in all rabbits. The vast majority of neovessels within the aortic wall were located in the adventitia opposite regions of thickening intimal plaque. The total number of PECAM-positive microvessels per section when averaged across all aortic slices was greater ($P < 0.05$) in control rabbits than in those given $\alpha_v\beta_3$-targeted fumagillin nanoparticles, particularly in the proximal half of the abdominal aorta, which displayed more prominent disease.

Duration of antiangiogenic effect after treatment with $\alpha_v\beta_3$-integrin-targeted fumagillin nanoparticles—In the next study, the duration of a single dose of $\alpha_v\beta_3$-targeted fumagillin nanoparticles was examined as a function of fumagillin dose (30 vs. 90 μg/kg) in animals continued and withdrawn from cholesterol diets following the start of treatment (Fig. 5). At baseline, the average percent signal enhancement from $\alpha_v\beta_3$-targeted paramagnetic nanoparticles did not differ between treatment groups and was similar to earlier studies [64]. Again, $\alpha_v\beta_3$-targeted paramagnetic contrast was diffusely distributed across and within slices, and the enhancement calculated represented the average of all aortic voxels rather than a threshold subset. MR neovascular signal did not differ between fat-fed animals switched to standard chow and those continuing on the cholesterol-enriched diet over the 4-week study, which reflected the marked and persistent serum cholesterol elevation and fatty liver disease observed in all animals continuing throughout the study.

As noted previously, angiogenesis contrast among animals receiving $\alpha_v\beta_3$-targeted fumagillin nanoparticles was decreased by approximately 50–75% relative to the control animals ($P < 0.05$). The decreased neovascular signal persisted through week 2. On week 3, aortic angiogenesis remained less than the control ($P < 0.05$) in both dietary groups, but the difference was smaller, indicating that the effect of the single dose of fumagillin was waning. By week 4, there was no difference in the MR neovasculature signal between control and fumagillin-treated rabbits regardless of diet or fumagillin dose from 30 to 90 μg/kg.

Antiangiogenic synergism of $\alpha_v\beta_3$-integrin-targeted fumagillin nanoparticles and atorvastatin—HMG-CoA reductase inhibitors have been proven to reduce cardiovascular risk [99], but their benefits may exceed the primary lipid-lowering effects. The pleiotropic benefits of statins have been attributed to antioxidant effects [100] diminished leukocyte-endothelial cell adhesion [101], attenuated macrophage activation and cytokine release [102], increased endothelial nitric oxide activity [103], and atherosclerotic plaque stabilization [104]. Pathological data from excised carotid arteries of patients treated for 3 months with statins have revealed a reduction in microvascular density, which was proposed as an explanation for the additional benefit of statins [105].

The three previous studies in hyperlipidemic rabbits demonstrated that $\alpha_v\beta_3$-targeted paramagnetic nanoparticles specifically home to angiogenic neovasculature in atherosclerotic aorta and deliver effective fumagillin therapy persisting for 3 weeks before recrudescing. The next but critical issue to be addressed was how to utilize and maintain the acute antiangiogenic benefits of fumagillin chronically in a clinically relevant care plan. The objective of this study was to determine whether the weak antian-giogenic response of statins would be adequate to sustain the acute antineovascular response of targeted fumagillin.

In a complicated 8-week experiment, the initial 4-week angiogenic response profile at baseline and following $\alpha_v\beta_3$-targeted fumagillin or control PFC nanoparticles did not differ from the previous 4-week experiment (Fig. 6). The neovascular integrated aortic signal of rabbits given atorvastatin alone did not differ from the nonstatin control counterparts. Animals receiving targeted fumagillin alone or in conjunction with oral statin had the same acute decrease in neovasculature at week 1, which returned to baseline levels at week 4.

However, following reinjection of targeted fumagillin in combination with continued dietary atorvastatin, the recrudescence of angiogenesis 4-week post-treatment was not observed, and a synergistic persistent antiangiogenesis effect, equivalent in magnitude to the 2-week response level, was observed. Dietary statin alone had no effect on angiogenesis in the second 4-week period (weeks 4–8 of study) nor did repeat treatment with fumagillin nanoparticles gain carry-over benefit from the prior treatment cycle. While atorvastatin alone exerted no significant effect on plaque angiogenesis in this short study, it is clear that dietary statin therapy synergistically extended the acute antineovascular benefits of $\alpha_v\beta_3$-targeted fumagillin PFC nanoparticles.

Conclusion

Clearly, perfluorocarbon nanoparticles are a versatile multimodal and theragnostic nanomedicine technology with anticipated clinical impact in the field of atherosclerosis and cancer. Homed to the $\alpha_v\beta_3$-integrin, this novel technology can detect and quantify nascent angiogenic expansion associated with minute tumors or early vascular disease. Although much work has been conducted with MRI, the diagnostic capability extends to ultrasound and nuclear imaging as well as hybrid applications. The drug delivery with these particles has been repeatedly shown for antiangiogenesis therapy, but also delivery of mellitin (i.e., NanoBees) in cancer, thrombolytics in acute ischemic stroke, and rapamycin following percutaneous angioplasty. This platform technology has advanced from the bench and to the clinic, where the first imaging results in man are highly anticipated.

Acknowledgments

Financial, equipment, or material support: AHS, PMW, SAW, SCD, and GL are supported by NCI, NHLBI, NIBIB (HL-78631, HL-73646, HL094470, and CA-119342) and Philips Healthcare. SAW and GML are scientific cofounders of Kereos, Inc.

References

1. Folkman J. Tumor angiogenesis: therapeutic implications. N Engl J Med. 1971; 285:1182–1186. [PubMed: 4938153]
2. Ferrara N, et al. Bevacizumab (Avastin), a humanized anti-VEGF monoclonal antibody for cancer therapy. Biochem Biophys Res Commun. 2005; 333:328–335. [PubMed: 15961063]
3. Cohen MH, et al. FDA drug approval summary: bevacizumab (Avastin) plus carboplatin and paclitaxel as first-line treatment of advanced/metastatic recurrent nonsquamous non-small cell lung cancer. Oncologist. 2007; 12:713–718. [PubMed: 17602060]
4. Cohen MH, et al. FDA drug approval summary: bevacizumab plus FOLFOX4 as second-line treatment of colorectal cancer. Oncologist. 2007; 12:356–361. [PubMed: 17405901]
5. Lang L. FDA approves sorafenib for patients with inoperable liver cancer. Gastroenterology. 2008; 134:379.
6. Rock EP, et al. Food and Drug Administration drug approval summary: sunitinib malate for the treatment of gastrointestinal stromal tumor and advanced renal cell carcinoma. Oncologist. 2007; 12:107–113. [PubMed: 17227905]
7. Eskens FA, Verweij J. The clinical toxicity profile of vascular endothelial growth factor (VEGF) and vascular endothelial growth factor receptor (VEGFR) targeting angiogenesis inhibitors; a review. Eur J Cancer. 2006; 42:3127–3139. [PubMed: 17098419]
8. Verheul HM, Pinedo HM. Possible molecular mechanisms involved in the toxicity of angiogenesis inhibition. Nat Rev Cancer. 2007; 7:475–485. [PubMed: 17522716]
9. Chen X, et al. MicroPET and autoradiographic imaging of breast cancer alpha v-integrin expression using ^{18}F- and ^{64}Cu-labeled RGD peptide. Bioconjug Chem. 2004; 15:41–49. [PubMed: 14733582]
10. Liu S, et al. Evaluation of a ^{99m}Tc-labeled cyclic RGD tetramer for noninvasive imaging integrin alpha(v)beta3-positive breast cancer. Bioconjug Chem. 2007; 18:438–446. [PubMed: 17341108]
11. Wilmes LJ, et al. AG-013736, a novel inhibitor of VEGF receptor tyrosine kinases, inhibits breast cancer growth and decreases vascular permeability as detected by dynamic contrast-enhanced magnetic resonance imaging. Magn Reson Imaging. 2007; 25:319–327. [PubMed: 17371720]
12. Liu G, et al. Dynamic contrast-enhanced magnetic resonance imaging as a pharmacodynamic measure of response after acute dosing of AG-013736, an oral angiogenesis inhibitor, in patients with advanced solid tumors: results from a phase I study. J Clin Oncol. 2005; 23:5464–5473. [PubMed: 16027440]
13. Leach MO, et al. The assessment of antiangiogenic and antivascular therapies in early-stage clinical trials using magnetic resonance imaging: issues and recommendations. Br J Cancer. 2005; 92:1599–1610. [PubMed: 15870830]
14. Hylton N. Dynamic contrast-enhanced magnetic resonance imaging as an imaging biomarker. J Clin Oncol. 2006; 24:3293–3298. [PubMed: 16829653]
15. Flacke S, et al. A novel MRI contrast agent for molecular imaging of fibrin: implications for detecting vulnerable plaques. Circulation. 2001; 104:1280–1285. [PubMed: 11551880]
16. Winter PM, et al. Molecular imaging of angiogenesis in nascent Vx-2 rabbit tumors using a novel alpha(nu)beta3-targeted nanoparticle and 1.5 Tesla magnetic resonance imaging. Cancer Res. 2003; 63:5838–5843. [PubMed: 14522907]
17. Schmieder A, et al. MR molecular imaging of melanoma angiogenesis with $\alpha_v\beta_3$-targeted paramagnetic nanoparticles. Magn Reson Med. 2005; 53:621–62. [PubMed: 15723405]
18. Sipkins DA, et al. Detection of tumor angiogenesis in vivo by alpha v beta 3-targeted magnetic resonance imaging. Nat Med. 1998; 4:623–626. [PubMed: 9585240]
19. Mulder WJ, et al. MR molecular imaging and fluorescence microscopy for identification of activated tumor endothelium using a bimodal lipidic nanoparticle. FASEB J. 2005; 19:2008–2010. [PubMed: 16204353]
20. Mulder WJ, et al. Lipid-based nanoparticles for contrast-enhanced MRI and molecular imaging. NMR Biomed. 2006; 19:142–164. [PubMed: 16450332]
21. Mulder WJ, et al. Early in vivo assessment of angiostatic therapy efficacy by molecular MRI. FASEB J. 2007; 21:378–383. [PubMed: 17202248]

22. Frias JC, et al. Recombinant HDL-like nanoparticles: a specific contrast agent for MRI of atherosclerotic plaques. J Am Chem Soc. 2004; 126:16316–16317. [PubMed: 15600321]
23. Krafft M. Fluorocarbons and fluorinated amphiphiles in drug delivery and biomedical research. Adv Drug Del Rev. 2001; 47:209–228.
24. De Nichilo M, et al. Granulocyte-macrophage and macrophage colony-stimulating factors differentially regulate alpha v integrin expression on cultured human macrophages. Proc Natl Acad Sci USA. 1993; 90:2517–2521. [PubMed: 7681600]
25. Helluin O, et al. The activation state of alpha v beta 3 regulates platelet and lymphocyte adhesion to intact and thrombin-cleaved osteopontin. J Biol Chem. 2000; 275:18337–18343. [PubMed: 10751402]
26. Itoh H, et al. The role of integrins in saphenous vein vascular smooth muscle cell migration. J Vasc Surg. 1997; 25:1061–1069. [PubMed: 9201167]
27. Carreiras F, et al. Expression and localization of alpha v integrins and their ligand vitronectin in normal ovarian epithelium and in ovarian carcinoma. Gynecol Oncol. 1996; 62:260–267. [PubMed: 8751559]
28. Kageshita T, et al. Differential clinical significance of alpha(v)Beta(3) expression in primary lesions of acral lentigi-nous melanoma and of other melanoma histotypes. Int J Cancer. 2000; 89:153–159. [PubMed: 10754493]
29. Weissleder R, et al. Size optimization of synthetic graft copolymers for in vivo angiogenesis imaging. Bioconjug Chem. 2001; 12:213–219. [PubMed: 11312682]
30. Ruoslahti E. Fibronectin and its receptors. Annu Rev Biochem. 1988; 57:375–413. [PubMed: 2972252]
31. Sadeghi MM, et al. Detection of injury-induced vascular remodeling by targeting activated alphavbeta3 integrin in vivo. Circulation. 2004; 110:84–90. [PubMed: 15210600]
32. Mattrey RF. The potential role of perfluorochemicals (PFCs) in diagnostic imaging. Artif Cells Blood Substit Immobil Biotechnol. 1994; 22:295–313. [PubMed: 8087248]
33. Mattrey R, et al. Perfluoroctylbromide: a liver/spleen = specific and tumor-imaging ultrasound contrast material. Radiology. 1982; 145:759–762. [PubMed: 7146409]
34. Lanza G, et al. A novel site-targeted ultrasonic contrast agent with broad biomedical application. Circulation. 1996; 94:3334–3340. [PubMed: 8989148]
35. Lanza G, et al. In vitro characterization of a novel, tissue-targeted ultrasonic contrast system with acoustic microscopy. J Acoust Soc Am. 1998; 104:3665–3672. [PubMed: 9857523]
36. Hall CS, et al. Experimental determination of phase velocity of perfluorocarbons: applications to targeted contrast agents. IEEE Trans Ultrason Ferroelec Freq Contr. 2000; 47:75–84.
37. Marsh JN, et al. Improvements in the ultrasonic contrast of targeted perfluorocarbon nanoparticles using an acoustic transmission line model. IEEE Trans Ultrason Ferroelectr Freq Control. 2002; 49:29–38. [PubMed: 11833889]
38. Hall C, et al. Temperature dependence of ultrasonic enhancement with a site-targeted contrast agent. J Acous Soc AM. 2001; 110:1677–1684.
39. Hughes MS, et al. Properties of an entropy-based signal receiver with an application to ultrasonic molecular imaging. J Acoust Soc Am. 2007; 121:3542–3557. [PubMed: 17552706]
40. Hughes MS, et al. Application of Renyi entropy for ultrasonic molecular imaging. J Acoust Soc Am. 2009; 125:3141–3145. [PubMed: 19425656]
41. Winter PM, et al. Improved molecular imaging contrast agent for detection of human thrombus. Magn Reson Med. 2003; 50:411–416. [PubMed: 12876719]
42. Winter P, et al. Improved paramagnetic chelate for molecular imaging with MRI. J Magn Magn Mater. 2005; 293:540–545.
43. Bachert P. Pharmacokinetics using fluorine NMR in vivo. Prog Nucl Magn Reson Spectrosc. 1998; 33:1–56.
44. Wolf W, et al. ^{19}F-MRS studies of fluorinated drugs in humans. Adv Drug Deliv Rev. 2000; 41:55–74. [PubMed: 10699305]
45. Kaneda MM, et al. Perfluorocarbon nanoemulsions for quantitative molecular imaging and targeted therapeutics. Ann Biomed Eng. 2009; 37:1922–1933. [PubMed: 19184435]

46. Lanza GM, et al. A novel site-targeted ultrasonic contrast agent with broad biomedical application. Circulation. 1996; 95:3334–3340. [PubMed: 8989148]
47. Yu X, et al. Molecular characterization of thrombus using bimodal ^{1}H/^{19}F MR imaging with a novel fibrin-targeted nanoparticulate contrast agent. Proc Int Soc Magn Reson Med. 2000; 8:465.
48. Morawski AM, et al. Quantitative “magnetic resonance immunohistochemistry” with ligand-targeted ^{19}F nanoparticles. Magn Reson Med. 2004; 52:1255–1262. [PubMed: 15562481]
49. Caruthers SD, et al. In vitro demonstration using ^{19}F magnetic resonance to augment molecular imaging with paramagnetic perfluorocarbon nanoparticles at 1.5 Tesla. Invest Radiol. 2006; 41:305–312. [PubMed: 16481914]
50. Neubauer AM, et al. Fluorine cardiovascular magnetic resonance angiography in vivo at 1.5 T with perfluorocarbon nanoparticle contrast agents. J Cardiovasc Magn Reson. 2007; 9:565–573. [PubMed: 17365236]
51. Waters EA, et al. Detection and quantification of angio-genesis in experimental valve disease with integrin-targeted nanoparticles and 19-fluorine MRI/MRS. J Cardiovasc Magn Reson. 2008; 10:43. [PubMed: 18817557]
52. Waters EA, et al. Detection of targeted perfluorocarbon nanoparticle binding using ^{19}F diffusion weighted MR spectroscopy. Magn Reson Med. 2008; 60:1232–1236. [PubMed: 18956417]
53. Haubner R, et al. Glycosylated RGD-containing peptides: tracer for tumor targeting and angiogenesis imaging with improved biokinetics. J Nucl Med. 2001; 42:326–336. [PubMed: 11216533]
54. Haubner R, et al. Radiolabeled alpha(v)beta3 integrin antagonists: a new class of tracers for tumor targeting. J Nucl Med. 1999; 40:1061–1071. [PubMed: 10452325]
55. Janssen ML, et al. Tumor targeting with radiolabeled alpha(v)beta(3) integrin binding peptides in a nude mouse model. Cancer Res. 2002; 62:6146–6151. [PubMed: 12414640]
56. McQuade P, et al. Evaluation of ^{64}Cu- and ^{125}I-radiola-beled bitistatin as potential agents for targeting alpha v beta 3 integrins in tumor angiogenesis. Bioconjug Chem. 2004; 15:988–996. [PubMed: 15366951]
57. Chen X, et al. MicroPET imaging of brain tumor angio-genesis with ^{18}F-labeled PEGylated RGD peptide. Eur J Nucl Med Mol Imaging. 2004; 31:1081–1089. [PubMed: 15118844]
58. Chen X, et al. Pharmacokinetics and tumor retention of ^{125}I-labeled RGD peptide are improved by PEGylation. Nucl Med Biol. 2004; 31:11–19. [PubMed: 14741566]
59. Chen X, et al. ^{18}F-labeled RGD peptide: initial evaluation for imaging brain tumor angiogenesis. Nucl Med Biol. 2004; 31:179–189. [PubMed: 15013483]
60. Onthank DC, et al. ^{90}Y and ^{111}In complexes of a DOTA-conjugated integrin alpha v beta 3 receptor antagonist: different but biologically equivalent. Bioconjug Chem. 2004; 15:235–241. [PubMed: 15025518]
61. Kong G, et al. Hyperthermia enables tumor-specific nanoparticle delivery: effect of particle size. Cancer Res. 2000; 60:4440–4445. [PubMed: 10969790]
62. Winter PM, et al. Molecular imaging of angiogenesis in early-stage atherosclerosis with alpha(v)beta3-integrin-targeted nanoparticles. Circulation. 2003; 108:2270–2274. [PubMed: 14557370]
63. Winter PM, et al. Minute dosages of alpha(nu)beta3-targeted fumagillin nanoparticles impair Vx-2 tumor angiogenesis and development in rabbits. FASEB J. 2008; 22:2758–2767. [PubMed: 18362202]
64. Winter P, et al. Antiangiogenic synergism of integrin-targeted fumagillin nanoparticles and atorvastatin in atherosclerosis. J Am Coll Cardiol Img. 2008; 1:624–634.
65. Schmieder AH, et al. Three-dimensional MR mapping of angiogenesis with {alpha}5{beta}1({alpha}{nu}{beta}3)-targeted theragnostic nanoparticles in the MDA-MB-435 xenograft mouse model. FASEB J. 2008; 22:4179–4189. [PubMed: 18697838]
66. Hu G, et al. Imaging of Vx-2 rabbit tumors with alpha(-nu)beta3-integrin-targeted 111In nanoparticles. Int J Cancer. 2007; 120:1951–1957. [PubMed: 17278104]
67. Lijowski M, et al. High sensitivity: high-resolution SPECT-CT/MR molecular imaging of angiogenesis in the Vx2 model. Invest Radiol. 2008; 43:100–111. [PubMed: 18197062]

68. Lanza GM, et al. Targeted antiproliferative drug delivery to vascular smooth muscle cells with a magnetic resonance imaging nanoparticle contrast agent: implications for rational therapy of restenosis. Circulation. 2002; 106:2842–2847. [PubMed: 12451012]
69. Soman N, et al. Synthesis and characterization of stable fluorocarbon nanostructures as drug delivery vehicles for cytolytic peptides. Nano Lett. 2008; 8:1131–1136. [PubMed: 18302330]
70. Crowder KC, et al. Sonic activation of molecularly-targeted nanoparticles accelerates transmembrane lipid delivery to cancer cells through contact-mediated mechanisms: implications for enhanced local drug delivery. Ultrasound Med Biol. 2005; 31:1693–1700. [PubMed: 16344131]
71. Cyrus T, et al. Intramural delivery of rapamycin with alphavbeta3-targeted paramagnetic nanoparticles inhibits stenosis after balloon injury. Arterioscler Thromb Vasc Biol. 2008; 28:820–826. [PubMed: 18292395]
72. Winter P, et al. Endothelial alpha(nu)beta(3)-Integrin targeted fumagillin nanoparticles inhibit angiogenesis in atherosclerosis. Arterioscler Thromb Vasc Biol. 2006; 26:2103–2109. [PubMed: 16825592]
73. Soman N, et al. A platform of molecularly targeted nanostructures for anticancer therapy with cytolytic peptides. J Clin Invest. 2009; 119:2830–2842. [PubMed: 19726870]
74. Marsh J, et al. Fibrin-targeted perfluorocarbon nanoparticles for targeted thrombolysis. Nanomedicine. 2007; 2:533–543. [PubMed: 17716136]
75. Liu S, et al. Structure of human methionine aminopepti-dase-2 complexed with fumagillin. Science. 1998; 282:1324–1327. [PubMed: 9812898]
76. Sin N, et al. The antiangiogenic agent fumagillin covalently binds and inhibits the methionine aminopeptidase, Me-tAP-2. Proc Natl Acad Sci USA. 1997; 94:6099–6103. [PubMed: 9177176]
77. Bergers G, et al. Effects of angiogenesis inhibitors on multistage carcinogenesis in mice. Science. 1999; 284:808–812. [PubMed: 10221914]
78. Castronovo V, Belotti D. TNP-470 (AGM-1470): mechanisms of action and early clinical development. Eur J Cancer. 1996; 32A:2520–2527. [PubMed: 9059342]
79. Konno H, et al. Efficacy of an angiogenesis inhibitor, TNP-470, in xenotransplanted human colorectal cancer with high metastatic potential. Cancer. 1996; 77:1736–1740. [PubMed: 8608571]
80. Shusterman S, et al. The angiogenesis inhibitor tnp-470 effectively inhibits human neuroblastoma xenograft growth, especially in the setting of subclinical disease. Clin Cancer Res. 2001; 7:977–984. [PubMed: 11309349]
81. Bhargava P, et al. A Phase I and pharmacokinetic study of TNP-470 administered weekly to patients with advanced cancer. Clin Cancer Res. 1999; 5:1989–1995. [PubMed: 10473076]
82. Kudelka AP, et al. Complete remission of metastatic cervical cancer with the angiogenesis inhibitor TNP-470. N Engl J Med. 1998; 338:991–992. [PubMed: 9527612]
83. Kudelka AP, et al. A phase I study of TNP-470 administered to patients with advanced squamous cell cancer of the cervix. Clin Cancer Res. 1997; 3:1501–1505. [PubMed: 9815836]
84. Logothetis CJ, et al. Phase I trial of the angiogenesis inhibitor TNP-470 for progressive androgen-independent prostate cancer. Clin Cancer Res. 2001; 7:1198–1203. [PubMed: 11350884]
85. Offodile R, et al. Regression of metastatic breast cancer in a patient treated with the anti-angiogenic drug TNP-470. Tumori. 1999; 85:51–53. [PubMed: 10228498]
86. Schmieder AH, et al. Molecular MR imaging of melanoma angiogenesis with alpha (v) beta (3)-targeted paramagnetic nanoparticles. Magn Reson Med. 2005; 53:621–627. [PubMed: 15723405]
87. Kim S, et al. Regulation of integrin alpha v beta 3-mediated endothelial cell migration and angiogenesis by integrin alpha 5 beta1 and protein kinase A. J Biol Chem. 2000; 275:33920–33928. [PubMed: 10944524]
88. Boudreau N, Varner J. The homeobox transcription factor Hox D3 promotes integrin alpha 5 beta 1 expression and function during angiogenesis. J Biol Chem. 2004; 279:4862–4868. [PubMed: 14610084]
89. Moreno PR, et al. Plaque neovascularization is increased in ruptured atherosclerotic lesions of human aorta: implications for plaque vulnerability. Circulation. 2004; 110:2032–2038. [PubMed: 15451780]

90. Moreno PR, et al. Neovascularization in human atherosclerosis. Circulation. 2006; 113:2245–2252. [PubMed: 16684874]
91. Virmani R, et al. Atherosclerotic plaque progression and vulnerability to rupture: angiogenesis as a source of intraplaque hemorrhage. Arterioscler Thromb Vasc Biol. 2005; 25:2054–2061. [PubMed: 16037567]
92. Bjornheden T, et al. Evidence of hypoxic areas within the arterial wall in vivo. Arterioscler Thromb Vasc Biol. 1999; 19:870–876. [PubMed: 10195911]
93. Boyle JJ, et al. Expression of angiogenic factor thymidine phosphorylase and angiogenesis in human atherosclerosis. J Pathol. 2000; 192:234–242. [PubMed: 11004701]
94. Khatri JJ, et al. Vascular oxidant stress enhances progression and angiogenesis of experimental atheroma. Circulation. 2004; 109:520–525. [PubMed: 14744973]
95. de Boer OJ, et al. Leucocyte recruitment in rupture prone regions of lipid-rich plaques: a prominent role for neovascularization? Cardiovas Res. 1999; 41:443–449.
96. Kolodgi F, et al. Eliminating plaque angiogenesis: reply. J Am Coll Cardiol. 2007; 50:1521.
97. Khurana R, et al. Role of angiogenesis in cardiovascular disease: a critical appraisal. Circulation. 2005; 112:1813–1824. [PubMed: 16172288]
98. Jain RK, et al. Antiangiogenic therapy for normalization of atherosclerotic plaque vasculature: a potential strategy for plaque stabilization. Nat Clin Pract Cardiovasc Med. 2007; 4:491–502. [PubMed: 17712362]
99. Pasternak RC, et al. ACC/AHA/NHLBI clinical advisory on the use and safety of statins. Circulation. 2002; 106:1024–1028. [PubMed: 12186811]
100. Girona J, et al. Simvastatin decreases aldehyde production derived from lipoprotein oxidation. Am J Cardiol. 1999; 83:846–851. [PubMed: 10190397]
101. Kimura M, et al. Effects of fluvastatin on leukocyte-endothelial cell adhesion in hypercholesterolemic rats. Arterioscler Thromb Vasc Biol. 1997; 17:1521–1526. [PubMed: 9301630]
102. Verhoeven BA, et al. Statin treatment is not associated with consistent alterations in inflammatory status of carotid atherosclerotic plaques: a retrospective study in 378 patients undergoing carotid endarterectomy. Stroke. 2006; 37:2054–2060. [PubMed: 16809559]
103. Laufs U, et al. Upregulation of endothelial nitric oxide synthase by HMG CoA reductase inhibitors. Circulation. 1998; 97:1129–1135. [PubMed: 9537338]
104. Sukhova GK, et al. Statins reduce inflammation in atheroma of nonhuman primates independent of effects on serum cholesterol. Arterioscler Thromb Vasc Biol. 2002; 22:1452–1458. [PubMed: 12231565]
105. Koutouzis M, et al. Statin treated patients have reduced intraplaque angiogenesis in carotid endarterectomy specimens. Atherosclerosis. 2007; 192:457–463. [PubMed: 17335827]

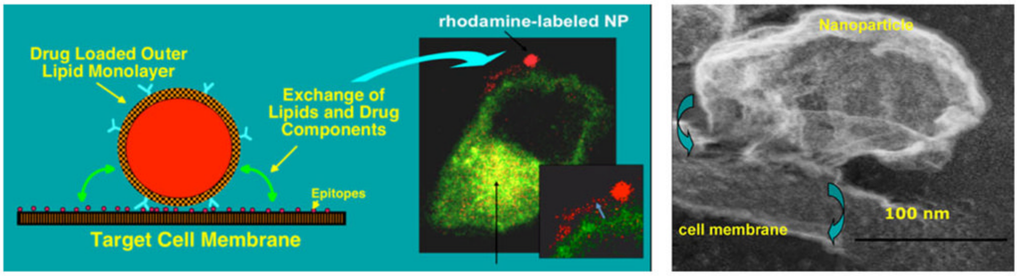

Fig. 1.

Left Contact facilitated drug delivery illustrated with rhodamine PFOB nanoparticle bound to C32 melanoma cell (transfected with Rab5 and Rab 7 GFP endocytic markers). *Right* Scanning electron micrograph of PFC nanoparticle forming a hemifusional complex with surface of endothelial cell. Lipids transfer to the target cell outer leaflet without ATP and require ATP to flip to the inner membrane. Reproduced with permission [68–70]

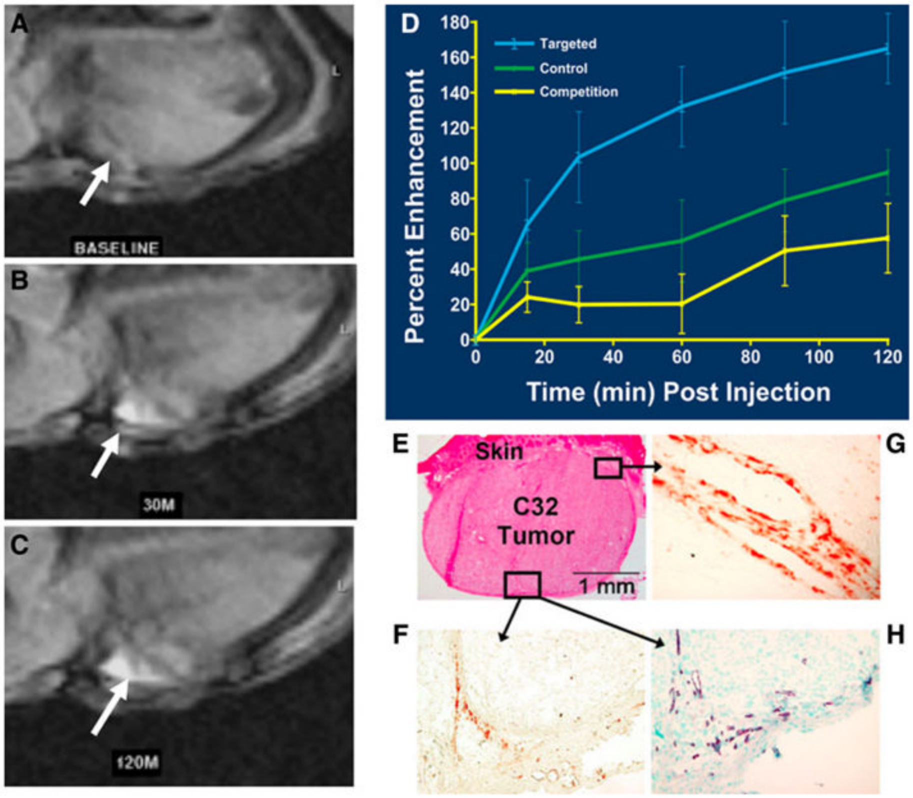

Fig. 2.

T1-weighted MR image (*axial view*, 1.5 T) of an athymic nude mouse before injection of $\alpha_v\beta_3$-targeted paramagnetic nanoparticles. **a** Baseline image of a C32 tumor that is difficult to detect. **b** 30-min post-injection. **c** 120-min post-injection. *White arrows* point to tumor in *panels* **a, b**, and **c**. Tumor diameter 2.5 mm. **d** Time course of MRI signal enhancement in tumor-bearing mice treated with $\alpha_v\beta_3$-targeted paramagnetic nanoparticles (*blue*), nontargeted contrast agent (*green*), or a competition procedure (*yellow*). T1-weighted signal enhancement in the targeted group was nearly twice that in the control animals given the untargeted agent ($P < 0.05$). Competitive blockage of $\alpha_v\beta_3$-integrin sites greatly diminished contrast ($P < 0.05$). **e–h** Immunohistochemistry revealing endothelial cell location and angiogenic vessel $\alpha_v\beta_3$-integrin expression along the periphery of C32 tumors and associated with infiltrating connective tissue. **e** H&E (×4). **f** β_3-integrin (×20). **g** β_3-integrin (×60) **h** PECAM-1 (×20, nuclear counterstained). Reproduced with permission [86]

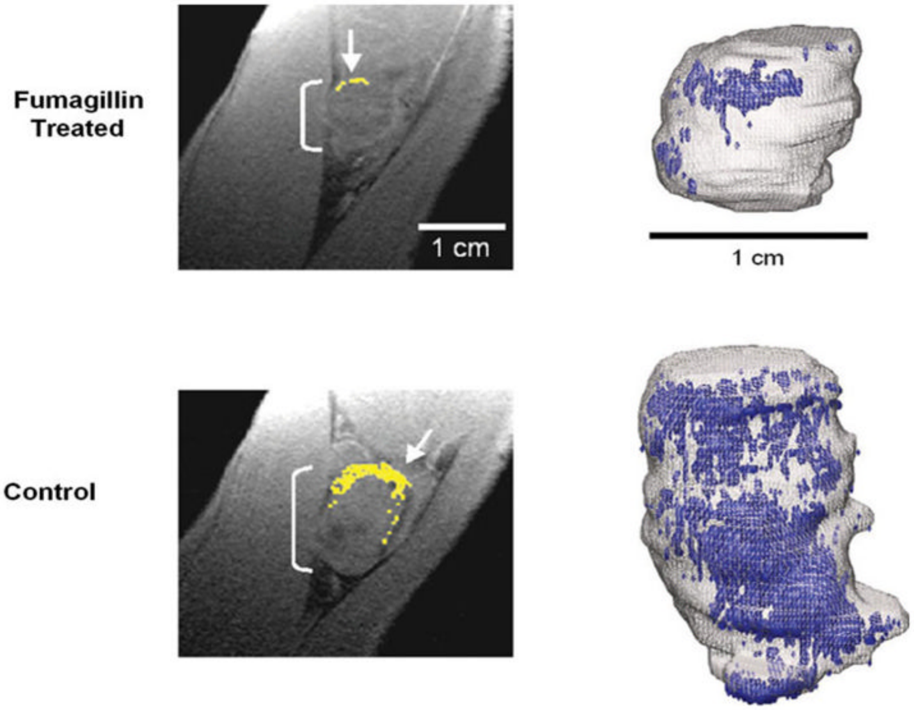

Fig. 3.

Diminished $\alpha_{\text{v}}\beta_3$ integrin contrast enhancement in T1-weighted, fat-suppressed, 3D gradient echo MR single slice images (250 ×250 μm, 500 μm slices, TR/TE = 40/5.6 ms, 65° flip angle, 1.5 T) in rabbits administered $\alpha_{\text{v}}\beta_3$-targeted fumagillin nanoparticles (*top*) versus those given $\alpha_{\text{v}}\beta_3$-targeted nanoparticles without drug (*bottom*). *Left*: Enhancing pixels, color coded in yellow (*arrows*), demonstrate sparse areas of angiogenesis in fumagillin-treated animal (*top*). *Right*: 3D neovascular maps of example Vx-2 tumors on day 16 following $\alpha_{\text{v}}\beta_3$-targeted fumagillin nanoparticles (*top*) versus $\alpha_{\text{v}}\beta_3$-nanoparticles without drug (*bottom*). Note the asymmetric distribution of angiogenic signal (color coded in *blue*) over the tumor surface in both the control and treated animals. Neovessel dense islands and the interspersed fine network of angiogenic proliferation over the tumor surface are diminished in rabbits receiving the targeted fumagillin treatment. Reproduced with permission [63]

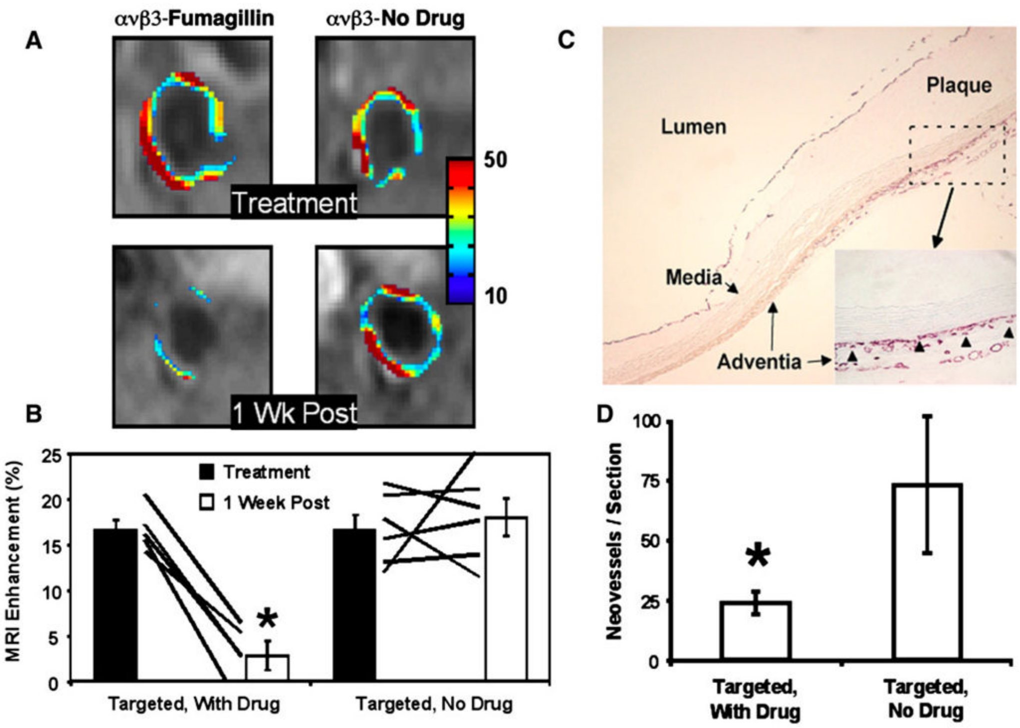

Fig. 4.

a MRI of abdominal aorta showing false-colored overlay of percent signal enhancement at time of treatment (*top*) and 1-week post-treatment (*bottom*). **b** Aortic MRI signal enhancement averaged over all imaged slices at the time of treatment (*filled bars*) and 1 week after treatment (*open bars*). Rabbits treated with $\alpha_v\beta_3$-targeted fumagillin nanoparticles had lower angiogenesis at 1 week compared with nanoparticles without fumagillin (* $P < 0.05$). The *solid lines* indicate individual animal response to treatment over the 7-day period. **c** PECAM-stained section (×4) of abdominal aorta from a hyperlipidemic rabbit displaying very early atherosclerotic changes in the adventitia, media, and plaque showing advential vasa vasorum expansion exclusively in region of plaque. Higher magnification inset (×20) shows microvessels were predominantly located in the adventitia associated with thickening neointima. *Arrowheads* illustrate the type of PECAM microvessels counted within each section to assess fumagillin antiangiogenic effects. **d** The number of neovascular vessels within the adventitia was reduced (* $P < 0.05$) in fumagillin-treated rabbits over the proximal half of the aorta (i.e., renal artery to diaphragm), which correlated with the region of greatest MR signal and fumagillin response in the imaging studies. Reproduced with permission [72]

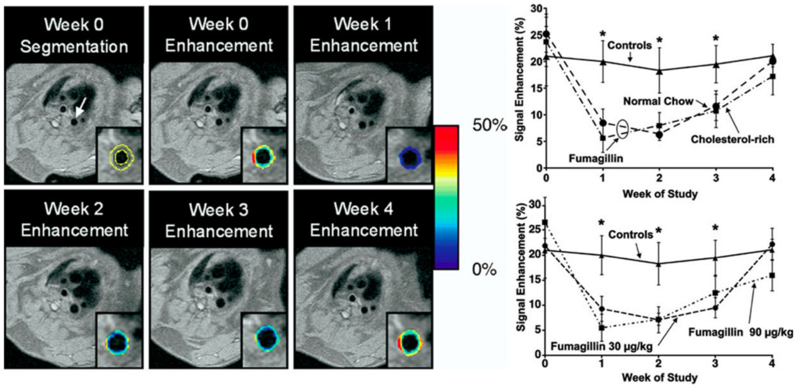

Fig. 5.

Left. (*Top*) Black blood image of the thoracic aorta (*arrow*) and segmentation of the vessel wall (*outlined* in *yellow*) is shown for the week 0 image. The color-coded overlay of signal enhancement (%) shows patchy areas of high angiogenesis. On the week 1 image, the signal enhancement has clearly decreased due to the antiangiogenic effect of targeted fumagillin treatment. (*bottom*) The level of signal enhancement gradually increases at weeks 2 and 3 after fumagillin treatment, until week 4, when the level of enhancement is practically identical to the week 0 image. *Right*. Aortic signal enhancement up to 4-week post-treatment with targeted fumagillin nanoparticles. *Top*: Fumagillin treatment at week 0 reduced angiogenesis compared to untreated controls, but withdrawing the high-cholesterol feed had no effect. *Bottom*: Fumagillin treatment at 30 versus 90 mg/kg produced identical responses (* $P < 0.05$). Reproduced with permission [64]

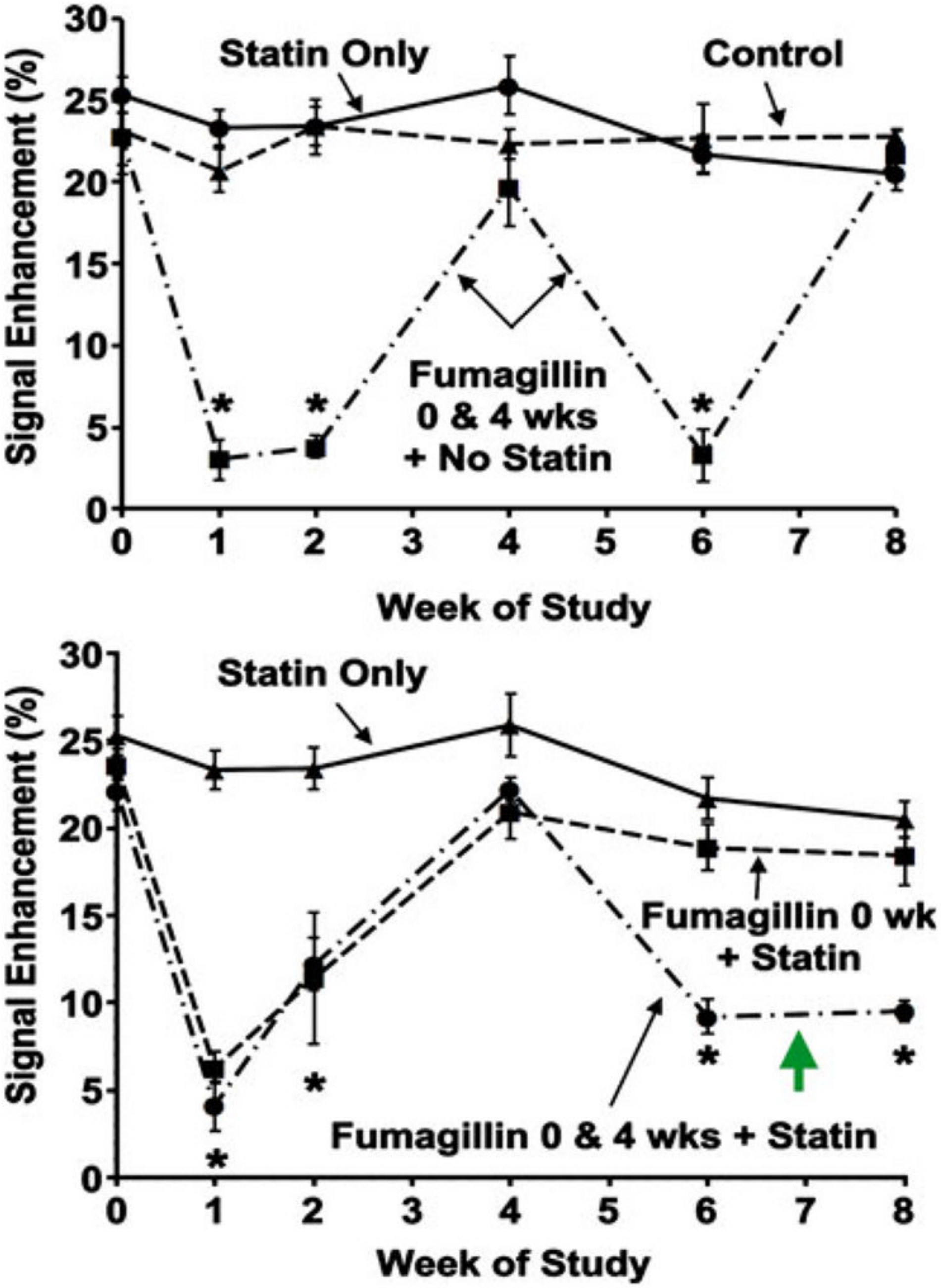

Fig. 6.

MR signal enhancement up to 8-week post-treatment with targeted fumagillin nanoparticles and/or oral atorvastatin. *Top*: Untreated and statin treated animals showed a constant level of angiogenesis in the aortic wall. Animals treated with targeted fumagillin nanoparticles at weeks 0 and 4 showed decreased angiogenesis (* $P < 0.05$) following each dose, which returned to baseline levels within 4 weeks. *Bottom*: The combination of two fumagillin doses and statin produced a sustained decrease in angiogenesis (* $P < 0.05$). *Green arrow* points to synergistic suppression of angiogenesis not achieved with statin or fumagillin alone (see *top panel*). Reproduced with permission [64]